JACS
JOURNAL OF THE AMERICAN CHEMICAL SOCIETY

Article

pubs.acs.org/JACS

Surface Charge Mapping with a Nanopipette

Kim McKelvey,[†] Sophie L. Kinnear,[†] David Perry,[†,‡] Dmitry Momotenko,[†] and Patrick R. Unwin*[,†]

[†]Department of Chemistry and [‡]MOAC Doctoral Training Centre, University of Warwick, Coventry, U.K. CV4 7AL

Supporting Information

ABSTRACT: Nanopipettes are emerging as simple but powerful tools for probing chemistry at the nanoscale. In this contribution the use of nanopipettes for simultaneous surface charge mapping and topographical imaging is demonstrated, using a scanning ion conductance microscopy (SICM) format. When a nanopipette is positioned close to a surface in electrolyte solution, the direct ion current (DC), driven by an applied bias between a quasi-reference counter electrode (QRCE) in the nanopipette and a second QRCE in the bulk solution, is sensitive to surface charge. The charge sensitivity arises because the diffuse double layers at the nanopipette and the surface interact, creating a perm-selective region which becomes increasingly significant at low ionic strengths (10 mM 1:1 aqueous electrolyte herein). This leads to a polarity-dependent ion current and *surface-induced rectification* as the bias is varied. Using distance-modulated SICM, which induces an alternating ion current component (AC) by periodically modulating the distance between the nanopipette and the surface, the effect of surface charge on the DC and AC is explored and rationalized. The impact of surface charge on the AC phase (with respect to the driving sinusoidal signal) is highlighted in particular; this quantity shows a shift that is highly sensitive to interfacial charge and provides the basis for visualizing charge simultaneously with topography. The studies herein highlight the use of nanopipettes for functional imaging with applications from cell biology to materials characterization where understanding surface charge is of key importance. They also provide a framework for the design of SICM experiments, which may be convoluted by topographical and surface charge effects, especially for small nanopipettes.

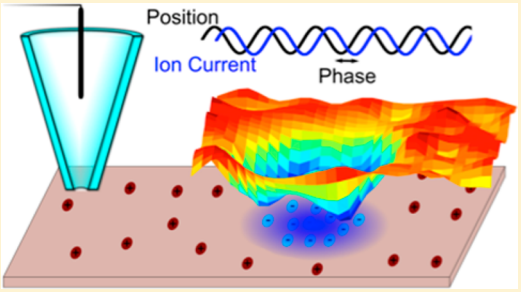

INTRODUCTION

Electrochemical measurements with, and control of, nanopipettes filled with electrolyte solution provide a platform for nanoscience, with myriad applications spanning analytical science,[1−5] materials characterization,[6−9] and live cell studies.[10] Nanopipettes used as the probe in scanning ion conductance microscopy (SICM) are particularly powerful as a means of imaging the local topography of substrates.[10−13] A bias is applied between a quasi-reference counter electrode (QRCE) in the nanopipette and another in the bulk of the solution to induce a direct ion current (DC) through the end of the nanopipette, as illustrated schematically in Figure 1. As the nanopipette−surface distance decreases, the solution resistance in the probe−surface gap increases which, in turn, reduces the ion current. This decrease in ion current is used as a noncontact signal to sense the nanopipette−surface distance and ultimately for topographical imaging,[14−16] proving particularly effective for soft samples.[10,12]

SICM is typically operated in aqueous solutions with relatively high ionic strength. Under these conditions the diffuse double layer (DDL) that forms at interfaces in solution is compressed (usually down to a (sub)nanometer level),[17] ensuring that nanopipette is relatively insensitive to surface charge effects and that the substrate topography is faithfully reproduced.[18] However, at lower electrolyte concentrations, the DDL characteristic length increases up to the several nanometer scale (in aqueous solutions), leading to surface charge effects such as ion current rectification (ICR) due to a polarity (bias)-dependent conductivity of the nanopipette, as seen in simple nanopipette studies of bulk solutions.[19−22] At small separation distances between a nanopipette and a charged substrate, the interaction of the respective DDLs similarly leads to changes in the ion current signal (*surface-induced rectification*)[23] opening up the prospect of surface charge mapping using SICM, as described herein. This is an important advance because there are relatively few techniques for probing and visualizing charge at interfaces. Although atomic force microscopy (AFM) can be used,[24−27] it employs a tip of (nominally) fixed charge that may change during a scan (e.g., by contamination or tip wear), and the force−distance characteristics are influenced by several forces as well as electrostatic forces. In contrast, as we highlight herein, the ion current through a nanopipette depends directly on the DDL at a charged surface and the applied potential can be tuned to optimize the response.

We use a nanopipette to investigate charged surfaces in electrolyte solutions at moderate aqueous ionic strength (10 mM 1:1 salt). We also take advantage of distance-modulated SICM,[28,29] where the probe−surface distance is oscillated with a small amplitude at a particular frequency to produce an alternating component (AC) in the ion current. We show that the ion current response (both DC and AC) is significantly affected by both substrate surface charge and the applied

Received: June 18, 2014
Published: September 2, 2014

   dx.doi.org/10.1021/ja506139u | J. Am. Chem. Soc. 2014, 136, 13735−13744

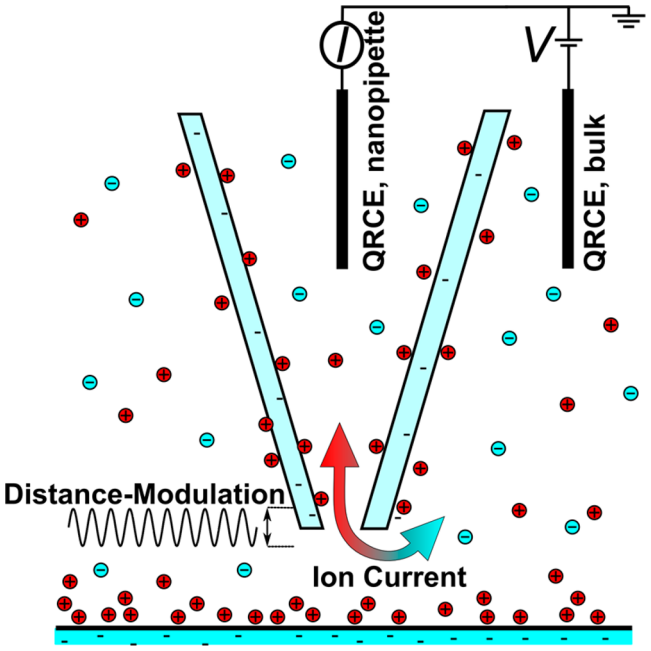

Figure 1. Schematic of an SICM probe, with one QRCE in a nanopipette and another in the bulk of the solution. A bias (V) is applied to the bulk QRCE, and the ion current (I) is measured at the QRCE in the nanopipette. A distance-modulated technique is used where a sinusoidal modulation is applied to the position of the nanopipette.

potential through approach curve measurements toward materials with different surface charge characteristics, namely glass, polystyrene, and (3-aminopropyl)triethoxysilane (APTES). In particular, we highlight that the *AC phase*, which has largely been overlooked in the SICM community, can give considerable information on the charge state of the surface. Experimental data are shown to be well represented with theoretical (finite element method) simulations. We use distance-modulated SICM to map the *topography and surface charge simultaneously* at model surfaces (polystyrene film with pinholes deposited on glass) and show that the phase signal, as well as the DC current, can distinguish between the two materials. We also demonstrate surface charge mapping of a soft positively charged polymer feature (poly-L-lysine), deposited as a small patch on a glass substrate. These model examples serve to illustrate the exciting possibility of using a nanopipette to map interfacial properties other than topography. We anticipate widespread applications in surface and interfacial science where knowledge of local surface charge would be hugely valuable for understanding interfacial processes.

METHODS AND MATERIALS

Solutions. Milli-Q reagent grade water (resistivity ca. 18.2 MΩ cm at 25 °C) was used for all solutions. KCl solutions (10 mM, pH 6.6, Sigma-Aldrich) were prepared for the SICM experiments. The pH values of electrolyte solutions were examined systematically before and after experiments to ensure stability, as pH could be a critical parameter controlling the charge properties of the interfaces, in particular those involving glass. Polystyrene (Sigma-Aldrich) was dissolved in chloroform (Fisher Scientific) at two different concentrations, one for creating a thick layer for SICM nanopipette approach tests (20 mg/mL) and one for dip-coating glass to create a thin (partial) film for imaging (0.66 mg/mL). A solution of (3-aminopropyl)triethoxysilane (APTES, Sigma-Aldrich) and toluene (2 μL/ml) was used for glass surface modification with APTES. To protonate the amino groups and produce a positively charged surface, all experiments carried out on APTES samples were performed in a slightly acidic solution of HCl (pH 3.4, Fisher Scientific) and KCl (9 mM). Consequently, the negative surface charge of the glass nanopipette in the studies at lower pH would be diminished. To create 5 μm diameter dots of poly-L-lysine (PLL) on glass, a solution of 0.25 mg/mL PLL with a supporting electrolyte of 25 mM KCl was used.

Nanopipettes. Nanopipettes of 60 nm radius with a half-cone angle of 3° (dimensions measured with a Zeiss Supra55VP field emission scanning electron microscope, FE-SEM) were pulled from borosilicate glass capillaries (o.d. 1.2 mm, i.d. 0.69 mm, Harvard Apparatus) using a laser puller (P-2000, Sutter Instruments, Pulling Parameters: Line 1: Heat 350, Fil 3, Vel 30, Del 220, Pul -, Line 2: Heat 350, Fil 3, Vel 40, Del 180, Pul 120). Tips visualized by FE-SEM were sputter coated with gold (10 nm thickness).

Substrates. Glass-bottomed Petri dishes with detachable coverslips (3512, WillcoWells) were used. Before use, the detachable coverslip was sonicated in acetone for 10 min followed by sonication in water for 10 min and plasma ashing for 1 min at 100 W in oxygen. These were then used immediately as glass samples or functionalized with either polystyrene or APTES. The polystyrene samples were either thick films prepared by evaporation of a solution of polystyrene in chloroform onto the glass, used for the nanopipette approach curve measurements, or dip coated for 30 s in a less concentrated polystyrene solution (see above), to produce a heterogeneous thin film with holes that exposed the glass in small regions. This created a surface of both neutral polystyrene and slightly negatively charged glass under the condition of the measurements (aerated, unbuffered, 10 mM KCl).[21−23,30] Silanized substrates were fabricated from glass coverslips immersed in the APTES/toluene solution for 30 min and then sonicated in chloroform to form a monolayer.[31]

A substrate containing patches of positively charged PLL on a glass sample was created by taking a clean glass Petri dish and depositing a spot of PLL for 3 min from a liquid meniscus formed in air at the end of a 5 μm diameter dual barreled-pipette, using the fabrication capabilities of scanning electrochemical cell microscopy.[32] This sample was then washed with water and dried under ambient conditions.

Instrumentation. The basic instrumentation has been described previously.[33,34] Briefly, the SICM probe was mounted on a 38 μm piezoelectric positioning stage (P-753-3CD, Physik Intrumente) for movement normal to the substrate (z-direction), while the sample was mounted on a two axis piezoelectric positioner system (Nano-BioS300, Mad City Labs Inc.) for lateral movement. The current was measured using a custom current-to-voltage converter. A lock-in amplifier (SR830, Stanford Research Systems) was used to generate the driving signal for the oscillation of the probe position and to determine the magnitude and phase of the AC ion current. Data recording, as well as the probe position and voltage output control, were performed using a LabVIEW (2013, National Instruments)-based program through a FPGA card (7852R, National Instruments). The lock-in amplifier phase calculation does not take into account the sign of the input signal, resulting in a 180° offset for negative current values compared to positive current values. Therefore, the phase at negative currents was translated by 180°, allowing phases at both positive and negative currents to be compared.

The nanopipette probe was filled with KCl solution, and an Ag/AgCl quasi-reference counter electrode (QRCE) was inserted. This comprised an AgCl-coated Ag wire.[35] The end of the nanopipette was placed close to the surface of interest that was immersed in KCl solution. A second Ag/AgCl QRCE was placed in the bulk of the solution. The QRCE in the bulk solution was biased with respect to the QRCE in the probe, and the resulting ion current was measured at the QRCE in the probe. All potentials quoted herein refer to the *potential of the QRCE in the nanopipette with respect to the bulk QRCE.*

SICM Approach Curves. The ion current, as a function of the probe−substrate distance, was measured at different potentials. To achieve this, the probe was oscillated at 288 Hz with 10 nm peak-to-peak amplitude and approached at 10 nm s^{-1} toward the surface of

dx.doi.org/10.1021/ja506139u | J. Am. Chem. Soc. 2014, 136, 13735−13744

interest with a bias of −0.2 V ($V_{QRCE,nanopipette} - V_{QRCE,bulk}$). Once the surface had been detected, through an increase in the AC current magnitude to 7 pA, the potential was switched to the potential of interest and the probe held stationary for 30 s for the ion current to stabilize. During this time the nanopipette−surface distance can change due to thermal expansion or retraction of the piezoelectric positioners (an effect called thermal drift).[36] However, as discussed in the Supporting Information, section SI-1, thermal drift is minimal for our experimental configuration (representing only 5 nm over 30 s) and so does not significantly affect the experimental results. The ion current response as the probe was moved away from the surface at 10 nm s^{-1} was then recorded. For some approach curves over glass, the tip (biased positively) was approached further toward the substrate, with the current observed to fall monotonically to low values before tip contact, indicating that the tip was well-aligned perpendicular to the surface.

SICM Maps. Two dimensional maps of a surface were generated in a hopping mode.[12,17,37] The SICM probe was approached, at 300 nm s^{-1}, to the surface of interest until the surface was detected, as an increase in the AC ion current magnitude to 4 pA, at multiple different lateral positions over the sample. The ion current and z-piezoelectric position was recorded during these hops, and the values at the closest approach to the surface were used to construct two-dimensional maps.

Atomic Force Microscopy. The height of the polystyrene/glass samples as revealed by SICM was compared to a section of the same sample imaged with atomic force microscopy (AFM) (Catalyst, Bruker-Nano) in contact mode using silicon tips on the nitride lever (SNL-10, Veeco). AFM images were processed using the scanning probe image processor program (SPIP 6.0.14, Image Metrology).

Simulations. Two-dimensional finite element method (FEM) simulations of the end of a 60 nm radius, 3° half-cone angle nanopipette in bulk and close to a charged surface were constructed to understand the theoretical basis of the ion current response. Simulations were constructed in Comsol Multiphysics using the transport of diluted species and electrostatics modules. Full details of the FEM simulations are available in Supporting Information section SI-2.

RESULTS AND DISCUSSION

The current−potential characteristics of a typical 60 nm radius nanopipette in bulk aqueous 10 mM KCl solution are shown in the Supporting Information, section SI-3, Figure S5. As expected, these nanopipettes show slight ICR due to the negative surface charge at the walls of the nanopipette,[21,22] with the current magnitude at positive values of the applied potential ($V_{QRCE,nanopipette} - V_{QRCE,bulk}$) being less than the current magnitude at negative potential values, as discussed in some detail in the literature[19,20,22,38,39] and briefly below. The additional effect of a charged surface on the DC and AC ion currents in SICM is investigated herein.

Approach Curves. The nanopipettes, operated in distance-modulation mode, were translated toward various surfaces in 10 mM KCl. The procedure outlined in Methods and Materials ensured that the nanopipette−surface distance was consistent at different potentials on a particular surface, with sets of curves obtained with one nanopipette. It should be noted, however, that the closest probe−surface distance is not the same for different surfaces due to the intrinsic charge characteristics of samples (vide infra). For convenience, probe−surface distances are assigned with respect to the point of closest approach, which can reasonably be expected to be within tens of nanometers of the surface itself, for all surfaces, as the ion current changes predominantly within a distance of a probe diameter from the substrate.[40] As could be expected, at a very small tip-to-substrate separation (data not shown), the drop in the ionic current was observed regardless of the nature of the substrate.

The ion current, normalized with respect to the ion current in bulk, for approach curves toward glass, polystyrene, and APTES are shown in Figure 2a−c, respectively (the raw ion current−distance curves are shown in Supporting Information, section SI-4 for reference). The glass provides a negatively charged surface (typically ca. −1 mC m^{-2} in 10 mM KCl, or −6 × 10^{-3} e nm^{-2}, where e is the electric charge of a proton),[21,23,41] the polystyrene a neutral surface, and APTES a positively charged surface.[42] Absolute values of a surface charge density

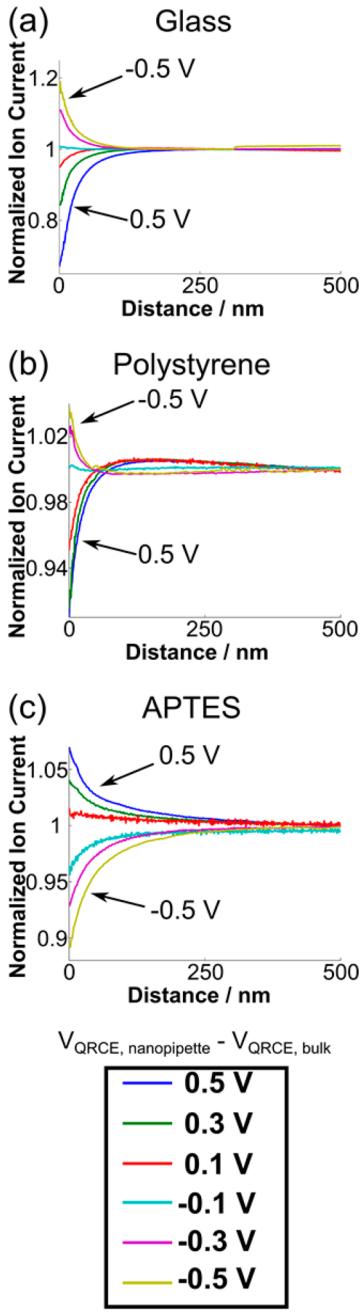

Figure 2. Normalized ion current as a function of probe−surface distance at different potentials over glass (a), polystyrene (b), and APTES (c) recorded in a 10 mM KCl solution for (a) and (b) and 9 mM KCl with 1 mM HCl solution for (c) with a 60 nm radius nanopipette, with an oscillation amplitude of 10 nm at 288 Hz.

dx.doi.org/10.1021/ja506139u | J. Am. Chem. Soc. 2014, 136, 13735−13744

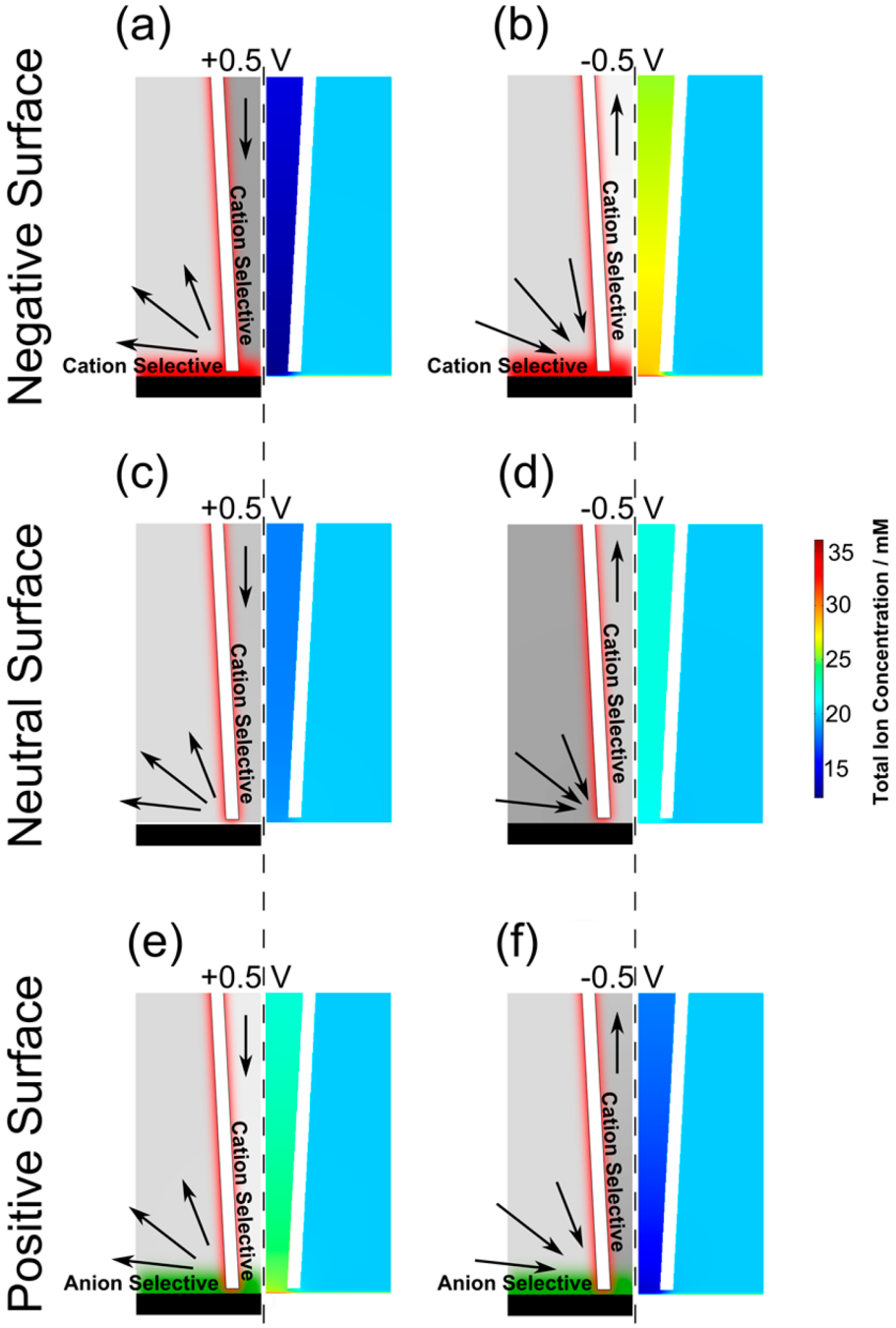

Figure 3. Schematics of cation mass transport flux (indicated by the arrows) and perm-selective regions (red, cation selective; green, anion selective) at the negatively charged nanopipette, and substrates of different charge (on the left of each part) and FEM simulation results (on the right of each part) of the resulting ion concentrations near the end of a nanopipette at surfaces. The nanopipette walls were 30 nm thick, and the nanopipette was 10 nm from the surface. Data are for a negatively charged surface (-5 mC m^{-2} or -3×10^{-2} e nm^{-2}) at applied potentials of 0.5 V (a) and -0.5 V (b), inside the nanopipette with respect to the bulk; a neutral surface at 0.5 V (c) and -0.5 V (d), inside the nanopipette with respect to the bulk; a positively charged (+5 mC m^{-2} or $+3 \times 10^{-2}$ e nm^{-2}) surface at 0.5 V (e) and -0.5 V (f), inside the nanopipette with respect to the bulk.

depend on a number of factors: the particular type of substrate (e.g., different types of glass), the surface pretreatment protocol employed, surface cleanliness, sample aging with time, and the surface environment (e.g., electrolyte concentration, pH, etc.). In this work, a moderate (and typical) surface charge among a wide range reported is chosen. On negatively charged glass (Figure 2a), the ion current shows an increase in magnitude as a function of decreasing nanopipette–surface distance at negative potential differences ($V_{QRCE,nanopipette} - V_{QRCE,bulk}$), while there is a decrease in current with smaller nanopipette–surface distance at positive potential differences. This pattern is similar on the polystyrene surfaces (Figure 2b), although the changes in the ion current with distance are greatly diminished compared to the behavior seen with the glass surface. Conversely, over the positively charged APTES surface (Figure 2c), an increase in ion current with decreasing nanopipette–surface distance is observed at positive ($V_{QRCE,nanopipette} - V_{QRCE,bulk}$) potentials, while there is a decrease in ion current with nanopipette–surface distance at negative potentials. Thus, the trend in the current–distance curves with respect to

dx.doi.org/10.1021/ja506139u | J. Am. Chem. Soc. 2014, 136, 13735–13744

potential is opposite to that seen with the negatively charged glass surface and neutral polystyrene-covered surface. The general observation is that the SICM ion current over charged interfaces depends on the bias polarity between the two QRCEs and the charge on the substrate, as recently reported, primarily through nanopore simulations.[23] In this contribution we describe *surface-induced rectification* at nanopipettes with a primary emphasis on high resolution scanning to probe and map surface charge effects with high sensitivity using both the DC and AC components of ion current.

The origin of the surface-induced polarity-dependent ion current is the interaction between the DDL at the tip and the DDL at the substrate, combined with the asymmetry of mass transport inside and outside the nanopipette. In the case of a negatively charged glass or quartz nanopipette in bulk solution, the interaction of the DDLs formed at the side walls of the nanopipette create a perm-selective region at the end on the nanopipette in which the migration and diffusion of cations dominates. Mass transport inside the nanopipette is limited by the conical geometry, while the outer space near the tip provides much faster transport due to a larger access angle. At a positive bias, cations are pushed from the nanopipette and the faster mass-transport rate outside the tip opening leads to the depletion of ion concentration inside the probe (as shown from FEM simulation results in Figure S3a of Supporting Information), giving rise to a low-conductance state and diminished ion current magnitude. At the opposite (negative) bias, cations are pushed toward the nanopipette at higher rates than they are transported inside, resulting in ion accumulation within the nanopipette (Supporting Information, Figure S3b), yielding a high-conductance state and an enhancement of the ion current magnitude. This effect is subtle with this size nanopipette and 10 mM KCl (Supporting Information Figure S3) yet detectable (Supporting Information Figure S5).

With a nanopipette approaching the charged surface, the rectifying scenarios are seriously affected by the presence of DDLs at the substrate, which exhibit perm-selective behavior toward cations or anions depending on the sign of the surface charge. It is therefore important to consider two coupled perm-selective regions: the one inside the nanopipette as in classical rectification and the one between the surface and the end of the nanopipette.

When the DDLs at the nanopipette and the surface consist of similar counter-ions (e.g., both the nanopipette and the substrate are negatively charged, Figure 3a,b), both the nanopipette and surface have similar perm-selective properties. In this case, cation selectivity of the interface gives rise to a build-up of high- and low-conductance states in the nanopipette, at negative and positive nanopipette bias, in a way very similar to that of classical ICR, but the accumulation/depletion of ions occurs not only inside the nanopipette but also in a perm-selective zone between the end of the nanopipette and the interface. Thus, ion concentration enhancement/depletion giving rise to the ICR effect is magnified (compare Figure 3 with Figure S3 in Supporting Information). As a consequence, and as shown by the simulations, a surface-mediated enhancement of local ion concentration (and hence ion current) occurs at negative bias (Figure 3b), and a surface-mediated decrease of ion current is expected at positive bias on the basis of the ion concentration profile in Figure 3a for the glass nanopipette approaching a glass substrate.

Over uncharged substrates there is a similar effect but of smaller magnitude. With charge solely on the nanopipette, there is only a weak cation-selective region between the probe and the substrate. As shown by FEM simulations, this causes the formation of low-conductance (Figure 3c) and high-conductance (Figure 3d) states inside the nanopipette and between the nanopipette and the surface, but the intensity of the effect is significantly smaller (less perturbation of the total ion concentration from the bulk value) compared to a negatively charged interface.

The significant influence of the surface charge for determining the rectifying characteristics in SICM is demonstrated in Figure 3e,f, for the case of the nanopipette tip in the vicinity of a positively charged interface. This case is especially interesting because the nanopipette and the interface exhibit the opposite perm-selective behavior, i.e., cation selectivity inside the nanopipette versus an anion-selective DDL at the surface. The inversion of rectifying properties with bias seen in Figure 2 can evidently be attributed to the inversion of the low- and high-conductance states in the nanopipette with respect to tip polarity. The anion-selective region at the surface plays the key role in this effect at this charge density (5 mC m^{-2}).

The simulation results (Figure 3) are in a good agreement with experimental results depicted in Figure 2 and with recent theoretical studies of surface-induced rectification which employed a simpler geometry and lower electrolyte concentration.[23] The agreement between experiment and the model is important because another recent report observing a polarity-dependent ion current signal over charged surfaces attributed the rectifying properties to the emergence of an electro-osmotic flow separation phenomenon.[43] The latter report described the surface-induced ion current enhancement at much higher electrolyte concentrations (150 mM NaCl), with much smaller nanopipettes (estimated 15 nm radius). Our results (in electrolyte solutions of relatively low ionic strength) demonstrate that rectification is due to the presence of a surface charge and diffusion/electromigration effects, which are sufficient to explain the experimental observations. In fact, as described in Supporting Information, section SI-2, we further incorporated electro-osmotic flow into our finite element simulations and found negligible effect on the ion current.[44,45] Thus, electro-osmotic effects play no part in surface-induced ICR phenomenon under the conditions of these experiments (tip size, bias, and electrolyte concentration).

Our studies now turn to the AC ion current components, induced by the oscillating probe, recorded in parallel with the ion current shown in Figure 2. As highlighted earlier, although distance-modulated SICM is becoming a widely used technique,[10] these parameters (especially the phase) have not been studied or analyzed in detail previously but provide rich information on interfacial properties (vide infra). Irrespective of the surface, the AC current amplitude increases as the nanopipette−surface distance decreases (see Supporting Information, section SI-5, which shows the AC ion current magnitude (normalized with respect to the bulk DC ion current) on glass, polystyrene, and APTES as a function of nanopipette−surface distance). The AC ion current magnitude at a particular distance represents the absolute change in ion current as the probe−surface distance is modulated (by 10 nm herein) at that distance and is therefore related to the magnitude of the slope of the DC ion current, with respect to distance. The AC magnitude thus tends to increase as the nanopipette approaches a surface. This signal is typically used as a means for the nanopipette to detect a surface,[10] and any surface charge effects are evidently obscured. However, the

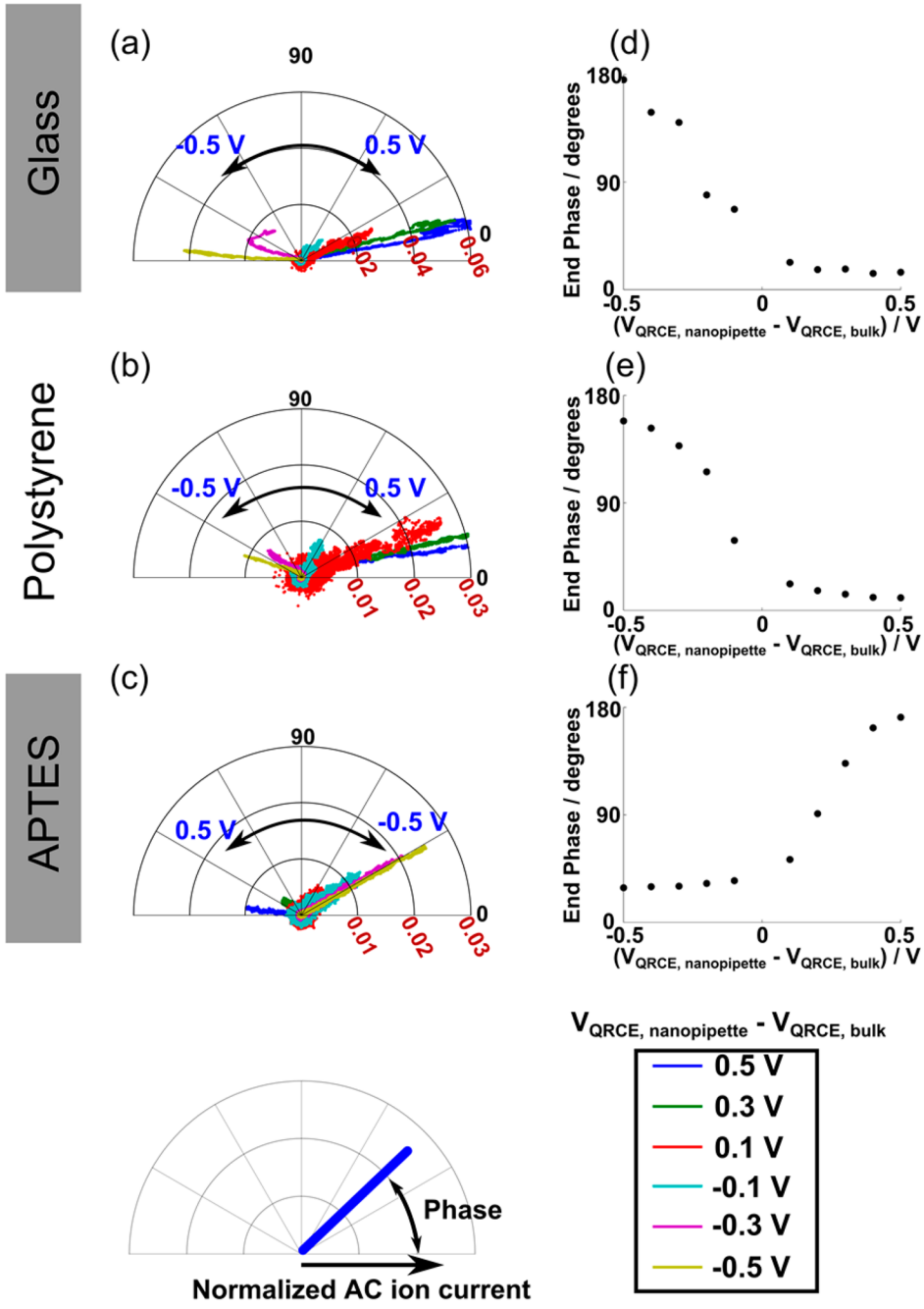

Figure 4. Polar plots, with the distance from the origin defined by the AC ion current magnitude normalized by the bulk DC ion current and angle defined by the ion current phase (as shown in the inset diagram at the bottom left) of the AC ion current over glass (a), polystyrene (b), and APTES (c) substrates. Data obtained in 10 mM KCl solution for (a) and (b) and 9 mM KCl with 1 mM HCl solution for (c) with a 60 nm radius nanopipette oscillated with an amplitude of 10 nm at 288 Hz. The phase value at the smallest nanopipette−surface distance with respect to the applied bias on glass (d), polystyrene (e), and APTES (f).

phase of the AC ion current can also be recorded, and we now show that this signal can be used to detect the surface charge with high sensitivity.

The periodic (time, t) change in the probe−surface distance, z (with amplitude A and frequency f) with respect to the interface, $z = A\sin(2\pi ft)$, leads to a harmonic oscillation in the ionic current, I_{AC}, (under the assumption of a small amplitude of distance modulation) $I_{AC} = kA\sin(2\pi ft + \varphi)$, where k is the slope of the current−distance curve. Hence, the harmonic ion current signal would be expected to be in phase with the driving vertical position oscillation (phase shift $\varphi = 0°$) at positive k (DC ion current drops in the vicinity of the substrate) or counterphase ($\varphi = 180°$) at negative k (ion current increase near the substrate), while at large separation distance, $k = 0$, i.e., there is no AC amplitude or phase shift. However, the experimental phase shifts measured in parallel with the DC and AC ion currents for glass, polystyrene, and APTES (as summarized in the polar plots in Figure 4a−c) are never strictly in phase or counterphase with respect to the driving oscillation and take intermediate values between 0° and 180°. Within the polar plots in Figure 4d−f, each data point from an approach curve is displayed at a coordinate with its radius

dx.doi.org/10.1021/ja506139u | J. Am. Chem. Soc. 2014, 136, 13735−13744

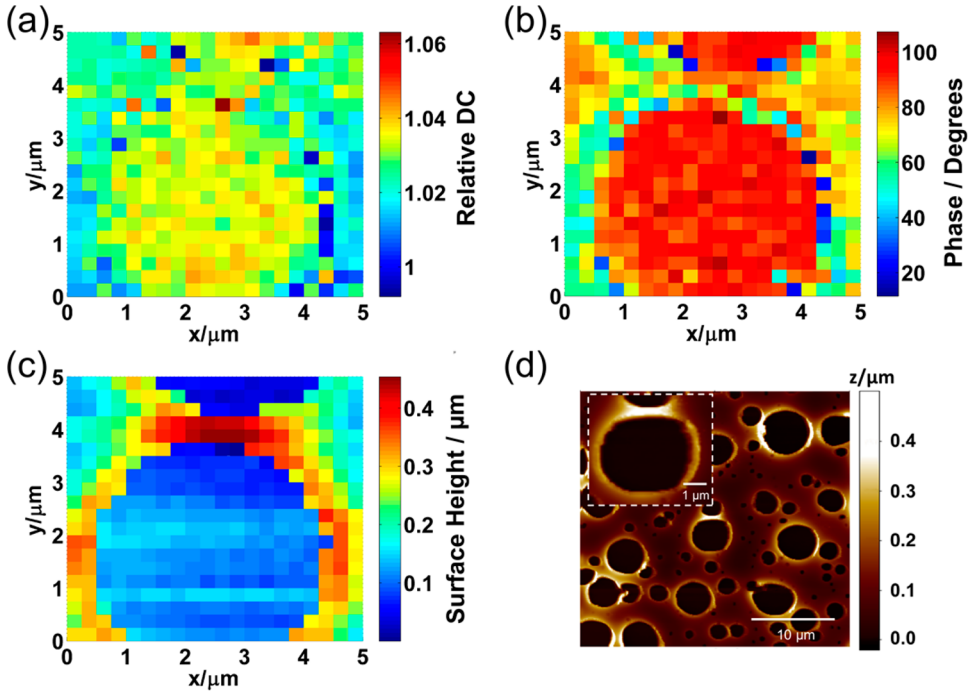

Figure 5. Two-dimensional hopping mode SICM images of a glass substrate partially covered with a thin polystyrene film. The images display the following ion current components recorded simultaneously, with an applied bias of 0.3 V: (a) normalized (with respect to bulk) DC ion current; (b) phase; (c) topography. A topographical image of a typical surface as determined by AFM is shown in panel d.

defined by the normalized AC ion current magnitude (the larger the current value, the closer the nanopipette to the surface), and the angle with respect to the positive horizontal axis defines the phase shift, φ. These features are labeled in Figure 4. At relatively large nanopipette-to-substrate distances, the AC ion current was negligible and so the traces were centered close to the origin (and largely contained experimental noise).

Interestingly, at closer nanopipette−surface distances, where an appreciable AC ion current was generated, the phase shift over each of the three surfaces correlates with the respective ICR behavior. Over all surfaces the phase was smallest (ca. 10° over glass and polystyrene, and ca. 30° over APTES) when the ion current magnitude decreased with decreasing nanopipette−surface distance ($V_{QRCE,nanopipette} - V_{QRCE,bulk}$ = 0.5 V over glass and polystyrene and at −0.5 V over APTES), while the highest φ values were associated with ion current enhancements at close nanopipette−surface distances, ($V_{QRCE,nanopipette} - V_{QRCE,bulk}$ = −0.5 V over glass and polystyrene, and 0.5 V over APTES).

These experimental findings indicate that the phase shift is intrinsically sensitive to the interfacial charge and therefore ionic transport properties at selective biases. The reason is that distance modulation of the nanopipette, when in close surface proximity, results in a periodic interaction of the DDLs of the nanopipette and the surface. On the basis of the results in Figure 3 (discussed above), this would tend to give rise to a periodic change in the conductance strength inside the nanopipette and in the probe−substrate region. The phase shift is then closely related to the time constant of ionic mass-transport required to change the conductance strength and is very bias sensitive.

It has recently been reported, by experiment and simulation of the bias-scan rate-dependent ion current in a nanopore in bulk solution,[46,47] that the high- and low-conductance states take 1−10 ms to build up (for nanopipettes and conditions similar those herein). Close to a surface where ICR is magnified (as discussed above), this time constant would increase. Thus, as the vertical modulation of the SICM tip in our experiments was 10 nm at 288 Hz, with a time constant for the peak-to-peak nanopipette oscillation of ca. 1.74 ms, the formation of ion depletion and ion accumulation zones is not likely to reach steady-state and lags the periodic perturbation. The resulting AC ion current is therefore phase shifted with respect to the driving oscillation, and this becomes especially significant when there is surface-induced charge accumulation in the nanopipette−surface region (negative nanopipette bias on glass and polystyrene, and positive nanopipette bias at APTES). Further details are given in Supporting Information, section SI-6.

Surface Charge Mapping. To demonstrate the newfound capabilities of distance-modulated SICM for high-resolution interfacial charge imaging, a surface consisting of a thin polystyrene film with holes revealing the glass substrate underneath was mapped in a hopping mode.[10,12] The nanopipette repeatedly approached the surface of the sample using the AC ion current amplitude with a set point of 4 pA (for positional feedback). Once the set point was reached, the nanopipette was retracted and then laterally moved by 250 nm to the next point, in this way forming a 5 μm by 5 μm image. The ion current (both DC and AC) was measured as a function of nanopipette vertical position during each approach, and the last data point (closest to the surface) of each was used to construct two-dimensional maps. As shown above (Figure 2) both the glass and polystyrene substrates cause DC ion current enhancement at the same polarity (negative values of $V_{QRCE,nanopipette} - V_{QRCE,bulk}$). Therefore, for imaging purposes, a fixed potential of −0.3 V was applied to the nanopipette, where the phase shift would be most sensitive to interfacial charge (vide infra).

dx.doi.org/10.1021/ja506139u | J. Am. Chem. Soc. 2014, 136, 13735−13744

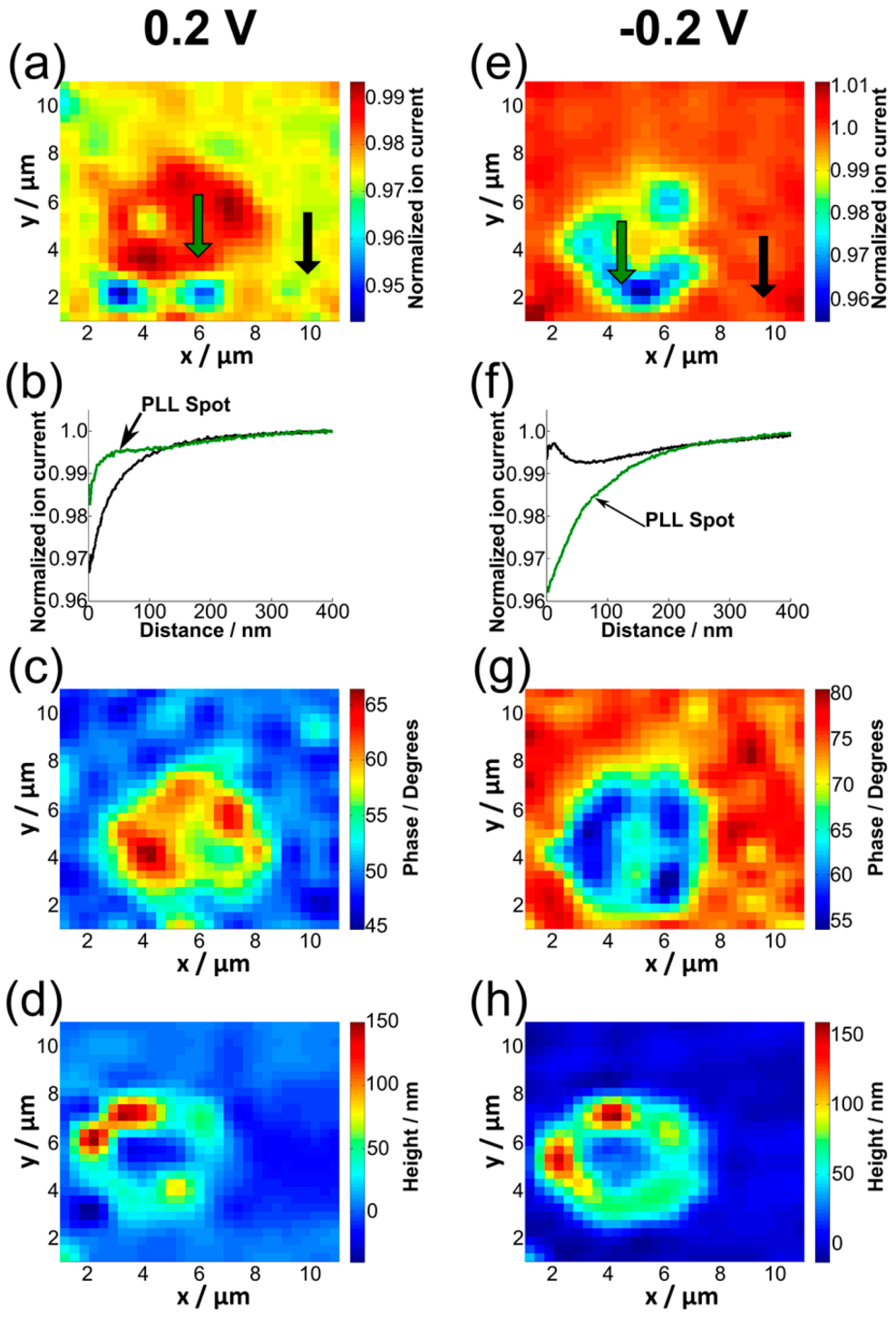

Figure 6. Hopping mode images, with 1 μm lateral step size, of a PLL spot (positively charged) on a glass substrate (negatively charged) with a bias of 0.2 V (left) and −0.2 V (right), applied to the QRCE in a 60 nm radius nanopipette with respect to a bulk QRCE in 10 mM KCl. The normalized ion current at the two different applied potentials is shown in panels a and e. Typical approach curves, at each potential, over the PLL spot (green) and over glass (black) are shown in panels b and f. Phase maps are shown in panels c and g. The surface topography, determined from the position that the surface was detected, is shown in panels d and h. Note that the 2D images are interpolated.

Figure 5a−c shows typical results: a normalized DC ion current map, a phase map, and topography map (determined from the position at which the surface was detected) *recorded simultaneously*. The normalized ion current reveals the glass exposed by a pore in the film due to the subtle difference in the response of the ion current during the approaches to the two materials, with the glass producing slightly higher surface ion currents compared to the polystyrene, as expected based on the approach curves and simulations in Figures 2 and 3.

The phase map (Figure 5b) also clearly reveals the glass spot but having much higher contrast compared to the DC ion current components. The phase shift tends toward 100° over glass and is surrounded by the polystyrene, where the phase value is lower. This indicates higher negative surface charge

dx.doi.org/10.1021/ja506139u | J. Am. Chem. Soc. 2014, 136, 13735−13744

density on the bare glass compared to the polystyrene-coated areas and demonstrates the efficiency of this approach to distinguish subtle surface charge heterogeneities at the nanoscale. Comparison of panels b and c of Figure 5 indicates that topography and surface charge are revealed with similar spatial resolution. A phase difference of >20° between the glass and polystyrene surfaces represents about 1 mC/m^2 with the surface charges assumed in this work. Given that the phase shift can be detected with a resolution of 1° (and that this could be further improved), this gives an indication of the sensitivity with which surface charge can be probed via phase detection. Moreover, the phase image exhibits similar spatial resolution to the topography image. Any ICR effect seen over the polystyrene is due to the double layer on the glass nanopipette alone, while for the glass there is a surface-induced contribution leading to a noticeably higher phase.

The topography, shown in Figure 5c, shows the flat glass surface surrounded by an area of polystyrene. This topography was confirmed by AFM (Figure 5d) which is seen to be in good agreement. Taken together, the data in Figure 5 illustrate that substrate topography and charge can be visualized simultaneously. This is because, as a function of nanopipette−surface distance, the AC magnitude (used as a set point) is relatively surface independent, at least on the scale of the topographical features in Figure 5. The ability to deconvolve surface charge and topography involves an interplay between the thickness of the double layer and the tip size. With decreasing tip size or ion concentration, as well as for substrates with extremely high surface charge density, the contribution of surface charge to the AC magnitude becomes more significant, resulting in a convolution of surface charge and topography. With a trend toward higher resolution imaging in SICM,[12,14,17] this is an effect that needs careful consideration if SICM is to measure true surface topography. The approach in this paper provides a framework for such an analysis and allows conditions to be identified where surface charge and topography can be resolved.

Finally, we mapped a soft polymeric spot with positive charge on a negatively charged background (glass with a 5 μm diameter spot of PLL) in a hopping mode, with a step size of 1 μm. Imaging was carried out twice with the same probe, first with a potential ($V_{QRCE,nanopipette} - V_{QRCE,bulk}$) of 0.2 V and then with a potential of −0.2 V. Figure 6 shows the results of the two maps, with the PLL spot on a glass surface apparent in both the normalized ion current (a and e), phase (c and g), and topography (d and h) maps. Similar to the charge mapping above, the AC ion current magnitude (4 pA), not shown, was used as the feedback parameter to detect the surface.

The normalized ion current, Figure 6, panels a and e, for 0.2 V and −0.2 V, respectively, both reveal the PLL spot. At 0.2 V ($V_{QRCE,nanopipette} - V_{QRCE,bulk}$) the DC ion current is higher over the PLL spot than over the glass, but at −0.2 V this is reversed, as expected due to the polarity dependence of the ion current response over the positively charged PLL and negatively charged glass surface. Typical approach curves over the PLL spot, and over the glass, at the two bias values are shown in Figure 6b,f. These approaches were taken at the marked positions in Figure 6a,e. At a bias of 0.2 V ($V_{QRCE,nanopipette} - V_{QRCE,bulk}$), the approaches over both glass and PLL decrease, but over PLL the current is higher. In contrast at −0.2 V ($V_{QRCE,nanopipette} - V_{QRCE,bulk}$), the ion current is higher over glass.

The phase shift of the ion current also shows the PLL spot very clearly. The difference in AC phase over the positively charged spot, compared to the surrounding negatively charged glass, is ca. 20° in both maps, but the sign of the change is bias-dependent. This makes the AC phase an especially sensitive and useful parameter for nanoscale surface charge measurements.

The topography, determined from the position that the surface was detected, is largely consistent at each bias (Figure 6d,h). This reveals that the PLL has deposited from the 5 μm diameter droplet in a "coffee" ring format.[48] The consistency of the topography at difference bias, together with the bias dependent phase (in particular) and ion current response, again highlights the capabilities of SICM for simultaneous topographical and charge mapping.

■ CONCLUSIONS

In solutions of moderate to low electrolyte concentration, the ion current (and alternating ion current) through a nanopipette is surface and potential dependent. This is primarily due to the creation of a perm-selective region between the nanopipette and the surface due to the interactions of the diffuse double layers at the substrate and the nanopipette, coupled with an asymmetry in mass-transport rates inside and outside the nanopipette. The ion current depends on the polarity. Indeed, the ion current can increase as the probe−surface distance decreases: at negative biases ($V_{QRCE,nanopipette} - V_{QRCE,bulk} < 0$) over negatively charged substrates and at positive biases ($V_{QRCE,nanopipette} - V_{QRCE,bulk} > 0$) over positively charged substrates. Significantly, for distance-modulation SICM there is a significant phase shift of the AC ion current component, which is highly sensitive to the diffuse double layer of the substrate surface.

Aided by these findings, we have shown that nanopipettes can be used to map the charge at solid−liquid interfaces in electrolyte solutions with the possibility of performing topographical and functional (surface charge heterogeneity) analysis simultaneously. This expands SICM beyond its main application of non-contact mapping of substrate topography and brings new multifunctional capability. In addition, our work has implications for the capability of SICM to map true surface topography, especially with very small tips. The analysis in this paper provides a guide for the design and execution of optimal SICM experiments, depending on the application and information sought. In this paper we have highlighted the ability of a nanopipette to detect surface charge variations semi-quantitatively for surfaces and interfaces with rather modest charge densities. With further simulations it should be possible to extract quantitative surface charge values with good precision and further optimize the technique. Practically, an important feature of the approach described is that the nanopipette in bulk solution can be checked regularly during a scan (especially in hopping mode where pixel level calibration is possible). The ability to check the probe and measure its charge characteristics in this way is particularly advantageous compared to other techniques for surface charge mapping such as AFM.

■ ASSOCIATED CONTENT

Supporting Information

Additional information, as noted in the text, on thermal drift, FEM simulations, the conductive characteristics of the nanopipettes, raw data for DC ion current approach curves, and AC magnitude approach curves. This material is available free of charge via the Internet at http://pubs.acs.org.

AUTHOR INFORMATION

Corresponding Author

P.R.Unwin@warwick.ac.uk

Notes

The authors declare no competing financial interest.

ACKNOWLEDGMENTS

We thank the European Research Council (ERC-2009-AdG247143-QUANTIF) and the EPSRC (through the MOAC DTC) for funding. We are grateful to Alex W. Colburn (University of Warwick) for custom built electronics.

REFERENCES

(1) Sa, N.; Baker, L. A. *J. Am. Chem. Soc.* **2011**, *133*, 10398−10401.
(2) Luo, L.; Holden, D. A.; White, H. S. *ACS Nano* **2014**, *8*, 3023−3030.
(3) Davenport, M.; Healy, K.; Pevarnik, M.; Teslich, N.; Cabrini, S.; Morrison, A. P.; Siwy, Z. S.; Létant, S. E. *ACS Nano* **2012**, *6*, 8366−8380.
(4) Morris, C. A.; Friedman, A. K.; Baker, L. A. *Analyst* **2010**, *135*, 2190−2202.
(5) Shen, M.; Ishimatsu, R.; Kim, J.; Amemiya, S. *J. Am. Chem. Soc.* **2012**, *134*, 9856−9859.
(6) Piper, J. D.; Li, C.; Lo, C.; Berry, R.; Korchev, Y.; Ying, L.; Klenerman, D. *J. Am. Chem. Soc.* **2008**, *130*, 10386−10393.
(7) Laslau, C.; Williams, D. E.; Travas-Sejdic, J. *Prog. Polym. Sci.* **2012**, *37*, 1177−1191.
(8) Ebejer, N.; Güell, A. G.; Lai, S. C. S.; McKelvey, K.; Snowden, M. E.; Unwin, P. R. *Annu. Rev. Anal. Chem.* **2013**, *6*, 329−351.
(9) Lai, S. C. S.; Macpherson, J. V.; Unwin, P. R. *MRS Bull.* **2012**, *37*, 668−674.
(10) Chen, C.; Zhou, Y.; Baker, L. A. *Annu. Rev. Anal. Chem.* **2012**, *5*, 207−228.
(11) Hansma, P. K.; Drake, B.; Marti, O.; Gould, S. A. C.; Prater, C. B. *Science* **1989**, *243*, 641−643.
(12) Novak, P.; Li, C.; Shevchuk, A. I.; Stepanyan, R.; Caldwell, M.; Hughes, S.; Smart, T. G.; Gorelik, J.; Ostanin, V. P.; Lab, M. J.; Moss, G. W. J.; Frolenkov, G. I.; Klenerman, D.; Korchev, Y. E. *Nat. Methods* **2009**, *6*, 279−281.
(13) Chen, C.-C.; Zhou, Y.; Baker, L. A. *ACS Nano* **2011**, *5*, 8404−8411.
(14) Gorelik, J.; Shevchuk, A. I.; Frolenkov, G. I.; Diakonov, I. A.; Lab, M. J.; Kros, C. J.; Richardson, G. P.; Vodyanoy, I.; Edwards, C. R. W.; Klenerman, D.; Korchev, Y. E. *Proc. Natl. Acad. Sci. U. S. A.* **2003**, *100*, 5819−5822.
(15) Nikolaev, V. O.; Moshkov, A.; Lyon, A. R.; Miragoli, M.; Novak, P.; Paur, H.; Lohse, M. J.; Korchev, Y. E.; Harding, S. E.; Gorelik, J. *Science* **2010**, *327*, 1653−1657.
(16) Korchev, Y. E.; Bashford, C. L.; Milovanovic, M.; Vodyanoy, I.; Lab, M. J. *Biophys. J.* **1997**, *73*, 653−658.
(17) Klenerman, D.; Korchev, Y. E.; Davis, S. J. *Curr. Opin. Chem. Biol.* **2011**, *15*, 1−8.
(18) Rheinlaender, J.; Geisse, N. A.; Proksch, R.; Schäffer, T. E. *Langmuir* **2011**, *27*, 697−704.
(19) Wei, C.; Bard, A. J.; Feldberg, S. W. *Anal. Chem.* **1997**, *69*, 4627−4633.
(20) Siwy, Z.; Heins, E.; Harrell, C. C.; Kohli, P.; Martin, C. R. *J. Am. Chem. Soc.* **2004**, *126*, 10850−10851.
(21) Momotenko, D.; Cortés-Salazar, F.; Josserand, J.; Liu, S.; Shao, Y.; Girault, H. H. *Phys. Chem. Chem. Phys.* **2011**, *13*, 5430−5440.
(22) White, H. S.; Bund, A. *Langmuir* **2008**, *24*, 2212−2218.
(23) Sa, N.; Lan, W.; Shi, W.; Baker, L. A. *ACS Nano* **2013**, *7*, 11272−11282.
(24) Manne, S.; Cleveland, J. P.; Gaub, H. E.; Stucky, G. D.; Hansma, P. K. *Langmuir* **1994**, *10*, 4409−4413.
(25) Heinz, W. F.; Hoh, J. H. *Biophys. J.* **1999**, *76*, 528−538.
(26) Miyatani, T.; Okamoto, S.; Rosa, A.; Marti, O.; Fujihira, M. *Appl. Phys. A: Mater. Sci. Process.* **1998**, *66*, S349−S352.
(27) Hillier, A. C.; Kim, S.; Bard, A. J. *J. Phys. Chem.* **1996**, *100*, 18808−18817.
(28) Shevchuk, A. I.; Gorelik, J.; Harding, S. E.; Lab, M. J.; Klenerman, D.; Korchev, Y. E. *Biophys. J.* **2001**, *81*, 1759−1764.
(29) Chen, C.; Baker, L. A. *Analyst* **2011**, *136*, 90−97.
(30) Powell, H. V.; Schnippering, M.; Mazurenka, M.; Macpherson, J. V.; Mackenzie, S. R.; Unwin, P. R. *Langmuir* **2009**, *25*, 248−255.
(31) Chauhan, A. K.; Aswal, D. K.; Koiry, S. P.; Gupta, S. K.; Yakhmi, J. V.; Sürgers, C.; Guerin, D.; Lenfant, S.; Vuillaume, D. *Appl. Phys. A: Mater. Sci. Process.* **2007**, *90*, 581−589.
(32) McKelvey, K.; O'Connell, M. A.; Unwin, P. R. *Chem. Commun.* **2013**, *49*, 2986−2988.
(33) Nadappuram, B. P.; McKelvey, K.; Al Botros, R.; Colburn, A. W.; Unwin, P. R. *Anal. Chem.* **2013**, *85*, 8070−8074.
(34) McKelvey, K.; Perry, D.; Byers, J. C.; Colburn, A. W.; Unwin, P. R. *Anal. Chem.* **2014**, *86*, 3639−3646.
(35) Snowden, M. E.; Güell, A. G.; Lai, S. C. S.; McKelvey, K.; Ebejer, N.; O'Connell, M. A.; Colburn, A. W.; Unwin, P. R. *Anal. Chem.* **2012**, *84*, 2483−2491.
(36) Kim, J.; Shen, M.; Nioradze, N.; Amemiya, S. *Anal. Chem.* **2012**, *84*, 3489−3492.
(37) Takahashi, Y.; Murakami, Y.; Nagamine, K.; Shiku, H.; Aoyagi, S.; Yasukawa, T.; Kanzaki, M.; Matsue, T. *Phys. Chem. Chem. Phys.* **2010**, *12*, 10012−10017.
(38) Umehara, S.; Pourmand, N.; Webb, C. D.; Davis, R. W.; Yasuda, K.; Karhanek, M. *Nano Lett.* **2006**, *6*, 2486−2492.
(39) Kovarik, M. L.; Zhou, K.; Jacobson, S. C. *J. Phys. Chem. B* **2009**, *113*, 15960−15966.
(40) Edwards, M. A.; Williams, C. G.; Whitworth, A. L.; Unwin, P. R. *Anal. Chem.* **2009**, *81*, 4482−4492.
(41) Behrens, S. H.; Grier, D. G. *J. Chem. Phys.* **2001**, *115*, 6716−6721.
(42) Van der Maaden, K.; Sliedregt, K.; Kros, A.; Jiskoot, W.; Bouwstra, J. *Langmuir* **2012**, *28*, 3403−3411.
(43) Clarke, R. W.; Zhukov, A.; Richards, O.; Johnson, N.; Ostanin, V.; Klenerman, D. *J. Am. Chem. Soc.* **2013**, *135*, 322−329.
(44) Wang, D.; Liu, J.; Kvetny, M.; Li, Y.; Brown, W.; Wang, G. *Chem. Sci.* **2014**, *5*, 1827.
(45) Powell, M. R.; Sa, N.; Davenport, M.; Healy, K.; Vlassiouk, I.; Létant, S. E.; Baker, L. A.; Siwy, Z. S. *J. Phys. Chem. C* **2011**, *115*, 8775−8783.
(46) Guerrette, J. P.; Zhang, B. *J. Am. Chem. Soc.* **2010**, *132*, 17088−17091.
(47) Momotenko, D.; Girault, H. H. *J. Am. Chem. Soc.* **2011**, *133*, 14496−14499.
(48) Yunker, P. J.; Still, T.; Lohr, M. A.; Yodh, A. G. *Nature* **2011**, *476*, 308−311.